Highlights

Turbulence characteristics and mixing properties of gravity currents over complex topography

- Experimental study of gravity currents over a complex topography through non-intrusive techniques.
- Turbulence and mixing characteristics of spatially developing downslope gravity currents.
- To what extent can a gravity current be compared to a katabatic wind?

Turbulence characteristics and mixing properties of gravity currents over complex topography

Abstract

Understanding gravity currents developing on complex topography, that involve turbulence and mixing processes on a wide range of spatial and temporal scales, is of importance for estimating near ground fluxes in oceanic and atmospheric circulation. We present experimental results, based on high resolution velocity and density measurements, of constant upstream buoyancy supply gravity currents flowing from a horizontal boundary onto a tangent hyperbolic shaped slope. The mean flow, the turbulence characteristics and mixing properties, the latter expressed in terms of mixing lengths and eddy coefficients, are determined, highlighting their dependency on topography. These mean flow and mixing characteristics are compared with the field measurements in katabatic winds of Charrondière et al., showing that the mean katabatic flow structure is substantially different from that of the upstream buoyancy supply gravity current. However interestingly, dimensionless mixing lengths and eddy coefficients compare well despite the difference in mean flow structure and a two order of magnitude difference in the Reynolds number.

Keywords: Gravity currents, experiments, non-uniform slope, topographic effects, turbulence and mixing

1. Introduction

Gravity currents are frequent in the natural environment with the density difference being due to temperature, salinity, dissolved substances, or particles within the flow. Examples of such currents in the atmosphere and oceans are sea breeze fronts (Simpson, 1997), katabatic winds (Fernando, 2010; Princevac et al., 2008; Brun et al., 2017; Charrondière et al., 2022), continental slope boundary currents (Gordon et al., 2009), turbidity currents (Meiburg and Keller, 2010) including avalanches (Hopfinger, 1983) and

exchange flows (Marino et al., 2005; Negretti et al., 2007; Nogueira et al., 2013). For these reasons investigations of gravity currents in the context of their many applications have been numerous and of interdisciplinary nature. Several studies have shown how the propagation of dense, bottom gravity currents is affected by topographic aspects (Cuthbertson et al., 2018; De Falco et al., 2021; Maggi et al., 2022), by sloping boundaries (Baines, 2005; Dai, 2014; Zemach et al., 2019; Ellison and Turner, 1959; Pawlak and Armi, 2000) as well as rapidly changing slopes (Negretti et al., 2017; Martin et al., 2019; Negretti et al., 2022). Most of these studies have focused on the mean flow dynamics and the related entrainment of ambient fluid that strongly affects the flow development and fluid properties. Entrainment is related with the type of interfacial instability (Fernando, 1991; Odier et al., 2014; Smyth et al., 2007) that also depends on initial conditions and slope angle (Negretti et al., 2017; Martin et al., 2019).

Gravity currents involve a large variety of different processes, e.g. flow instabilities, boundary layers, vortices and internal waves, which occur in very localized regions, so that they cannot be resolved in oceanic and atmospheric circulation models (Laanaia et al., 2010).Since these currents affect the general circulation (Danabasoglu et al., 2010), a parametrization of their effect is necessary, which requires the determination of the involved turbulent and mixing processes.

Modern experimental techniques allow high quality, quantitative measurements of the mean flow development and entrainment, the turbulence characteristics, and internal mixing. Measurements of eddy coefficients and mixing lengths have been conducted in the outer part of a gravity current by Odier et al. (2009) and in lock exchange gravity currents by Balasubramanian and Zhong (2018); Agrawal et al. (2021); Mukherjee and Balasubramanian (2020, 2021). Measurements in katabatic winds on glaciers and alpine slopes have been performed by Princevac et al. (2008); Monti et al. (2014); Charrondière et al. (2021), who focused on mean flow oscillations and turbulence characteristics and, more recently, on mixing length and eddy coefficients (Charrondière et al., 2022).

Here, we present results from laboratory experiments of continuously supplied saline gravity currents flowing onto a complex topography of tangent hyperbolic shape that reproduces a typical alpine topography (Brun et al., 2017). Emphasis is placed on the turbulence and mixing characteristics in the different regions of the gravity current down the slope. Comparison of the present results with those obtained in the laboratory by Odier et al.

(2012) and by Charrondière et al. (2022) in katabatic winds is performed. The latter is of particular interest because Reynolds numbers and scales are widely different. Furthermore, most of the experimental data of katabatic winds have been obtained in a limited region above the maximum-wind-speed height where mixing lengths increase with height. Thus, laboratory results can shed new light on katabatic wind mixing behaviour.

The paper is organized as follows: the essential details on of the experimental apparatus and measurements techniques are given in Sec.2, including a general description of the flow development. Results of the mean flow development, mixing properties and Reynolds stresses are discussed in Sec.3. A comparison of some mean flow, mixing length and eddy coefficients of the present experiments with previous studies (Odier et al., 2012) and especially with the katabatic wind results of Charrondière et al. is presented in Sec.4. Sec.5 summarizes the results and includes concluding remarks.

2. Experimental design

The experiment, sketched in figure 1a and described in detail elsewhere (Negretti et al., 2017; Martin et al., 2019), consists of a saline gravity current initiated by injecting a constant flow rate Q_0 upstream of a 25cm wide and 160cm long horizontal channel within a lighter ambient fluid (ethanol solution for refractive index matching). The horizontal channel is followed by a hyperbolic tangent profiled slope boundary (cf. figure 1b), defined as:

$$y = \frac{h_c}{2}(1 - tanh(x)), \qquad \theta = atan(-\frac{h_c}{2}(1 - tanh(x^2))) \tag{1}$$

No return flow and a constant total water depth of $h = 20 \pm 0.5$cm in the initial horizontal channel were assured by evacuating the same volume as supplied at the downstream end of the experimental channel.

Fig.2 presents one series of snapshots of one experiment with dye added in the saline water ($D5_2$, cf. table 1) after the current has reached stationary conditions (i.e. after the initial passage of the gravity current head). Two different types of shear instabilities at the interface between the dense flow and the ambient fluid can be recognized: Holmboe instability (HI) near slope begin, followed by Kelvin–Helmholtz instabilities (KHI) on the steepest part of the slope. The final portion and the downstream part of the slope are characterized by the collapse of the KHIs which generate a turbulent (mixed) shear layer (TSL) with an intermediate upper density layer.

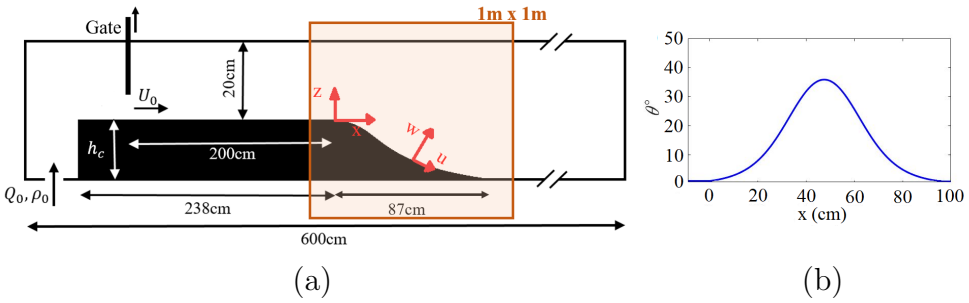

Figure 1: a) Schematic side-view of the tank used to perform laboratory experiments with the main geometrical features and the notations. b) Slope angle evolution along the x (down slope) direction.

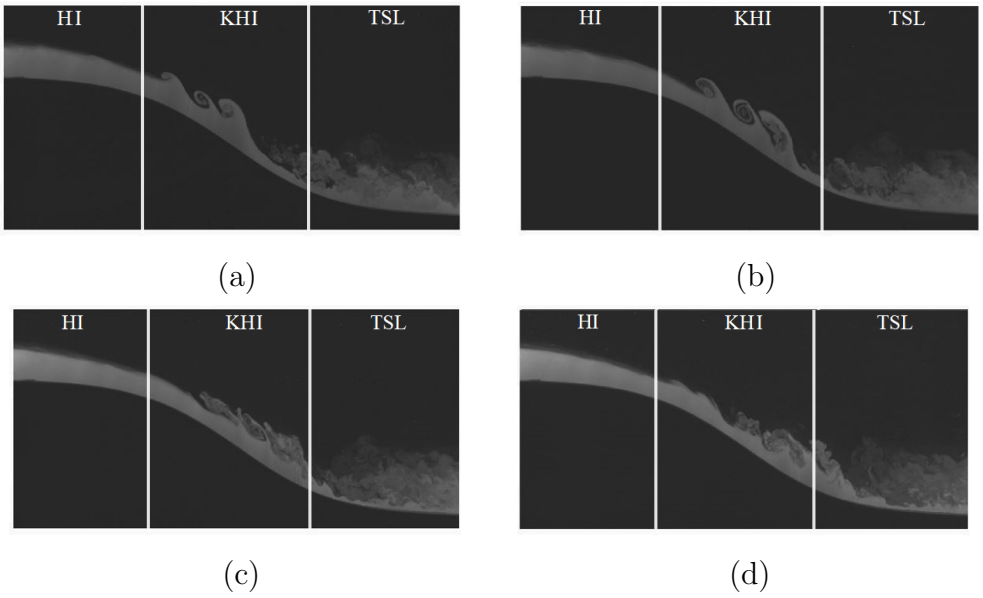

Figure 2: Instantaneous images of dye visualizations of a gravity current with $q_0 = 45.76\text{cm}^2\text{s}^{-1}$ and $g_0' = 5\text{cm s}^{-2}$. (a) $t = t_0$; (b) $t = t_0 + 0.01$s; (c) $t_0 + 0.02$s and (d) $t_0 + 0.03$s. Three different zones can be defined that are characterized by different interface instabilities: Holmboe instability (HI) near slope begin, Kelvin–Helmholtz instability (KHI) at steep slope and the final area of KHI collapse to a turbulent (mixed) shear layer (TSL).

Table 1: Parameters of the experiments conducted, where q_0 is the dense flow rate per unit width, g_0' the reduced gravity, $Re_0 = q_0/\nu$ is the inlet Reynolds number, $B_0 = q_0 g_0'$ is the initial buoyancy flux and h_{0i} is the initial height of the dense current in the horizontal part of the channel.

Run	$q_0(\mathrm{cm^2 s^{-1}})$	$g_0'(\mathrm{cm\ s^{-2}})$	Re_0	$B_0(\mathrm{cm^3 s^{-3}})$	$h_{0i}(\mathrm{cm})$
$R5_1$	32.28	5	3200	160	6
$R5_2$	45.76	5	4600	225	6.7
$R5_3$	57.24	5	5700	280	7.5
$R10_1$	32.28	10	3200	320	5.8
$R10_2$	45.76	10	4600	460	6.3
$R10_3$	57.24	10	5700	570	7
$R15_1$	32.28	15	3200	485	5.7
$R15_2$	45.76	15	4600	685	6
$R15_3$	57.24	15	5700	860	6.4
$D5_1$	32.28	5	3200	160	6
$D5_2$	45.76	5	4600	225	6.7
$D5_3$	57.24	5	5700	280	7.5

A total of 12 experiments have been performed by varying the initial density difference $\Delta\rho$ between the current and the ambient water and Q_0 (see table 1). The optical non-intrusive experimental technique PIV was adopted to measure the instantaneous velocity field in 9 experiments, while the fluorescent dye was added to the saline injected solution to determine the local relative density difference in further 3 experiments for evaluating the gradient Richardson number (cf. table 1).

For the PIV measurements, a CCD camera (1200x1600 pixels) was used to acquire the experimental images with an acquisition frequency of 23.23Hz. The camera allowed to record the whole slope field with an image size of 1m×1m. Each vector of the resulting field represents an area of approximately 0.23cm ×0.23cm. Further details on the PIV procedure are given in Negretti et al. (2007); Martin et al. (2019).

To estimate relative averaged density profiles, a local calibration procedure taking into account the light absorption of Rhodamine 6G added to the injected saline water has been adopted. Details of the procedure can be found in Negretti et al. (2008).

3. Experimental results

3.1. Mean flow development and entrainment

The along-slope mean velocity u and slope normal velocity w have been measured at three downstream positions x and are processed in experiments $R5_2$, $R15_2$ and $R15_3$ that are representative of all the experiments conducted. These show how a change in g'_0 and q_0 affect the flow. As in Negretti et al. (2017) and Martin et al. (2019), the flow distance x has been normalized by h_{0i}, the initial mean height of the dense current at slope begin, i.e. $x^* = x/h_{0i}$.

Fig.3 shows time-averaged along-slope velocity $\langle u \rangle$ and slope normal velocity $\langle w \rangle$ at three positions $x^* = 1$, $x^* = 7$ and $x^* = 11$ indicated by the continuous vertical black lines in Fig.3a. Upstream of the slope, the current has a constant $\langle u \rangle$ as long as the change in the bottom inclination does not affect the flow. Then, $\langle u \rangle$ increases until KHI develop, which cause the slow down of the current followed by a nearby maximum constant velocity, which is reached from $x^* \approx 7$ as seen the in the insets in Fig.4.

Fig.3b-d show the $\langle u \rangle$ velocity profile and Fig.3c-g the slope normal velocity distribution $\langle w \rangle$ at $x^* = 1$ (a,d), $x^* = 7$ (b,e) and $x^* = 11$ (c,f). The different symbol colors indicate different experiments, while the symbol shape refers to the position x^*.

In Fig.3a-c all the experiments show velocity profiles $\langle u \rangle$ similar to that of a plane turbulent wall jet (Eriksson et al., 1998) as has also been observed by Buckee et al. (2001) and Ottolenghi et al. (2016). The height where maximum velocity occurs is conditioned by interfacial drag. The velocity maximum moves closer to the bottom as x^* increases. Fig.3d-f shows the time-average vertical velocity $\langle w \rangle$. At $x^* = 1$ $\langle w \rangle$ is negative from the slope bottom up to the shear layer where it tends to zero. The behaviour is opposite at $x^* = 7$, where the slope is steepest with $\langle w \rangle$ being negative in the outer part of the current and in the ambient fluid. Further downstream at $x^* = 11$ $\langle w \rangle$ weakly decreases with increasing z.

In order to highlight more clearly the change in flow structure with downstream distance it is of interest to present velocities in dimensionless form. Fig.4 shows the variation along $z/z_{0.5}$ of the dimensionless longitudinal velocity $\langle u \rangle / \langle u_m \rangle$ (open symbols) and of the normal component $\langle w \rangle / \langle u_m \rangle$ (closed symbols) for experiments $R5_2$ (a) and $R15_3$ (b), where $\langle u_m \rangle$ is the maximum mean velocity, shown in the insets, and $z_{0.5}$, is the distance from the boundary where the velocity $\langle u \rangle$ is $\langle u_m \rangle / 2$. The maximum mean velocity, $\langle u_m \rangle$,

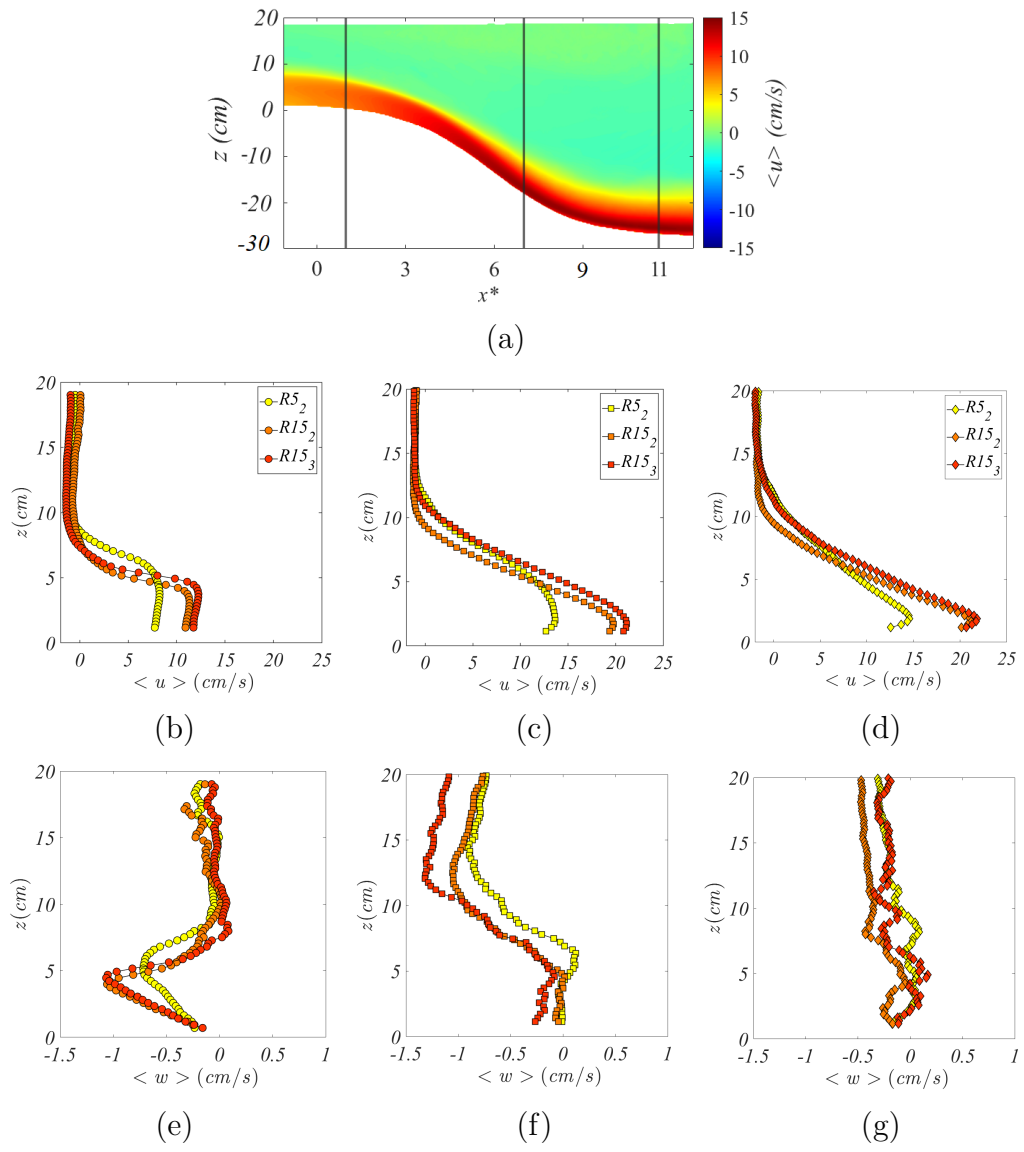

Figure 3: Time-averaged along-slope velocity $\langle u \rangle$ and slope normal velocity $\langle w \rangle$ at positions $x^* = 1, 7, 11$ for experiments $R5_2, (b-e)$, $R15_2, (c-f)$ and $R15_3, (d-g)$; (a), color plot of velocity $\langle u \rangle$ vs x^* for $R15_2$ with the vertical continuous lines indicating the positions $x^* = 1$, $x^* = 7$ and $x^* = 11$ where the time-averaged streamwise velocity profiles and the vertical velocity have been measured.

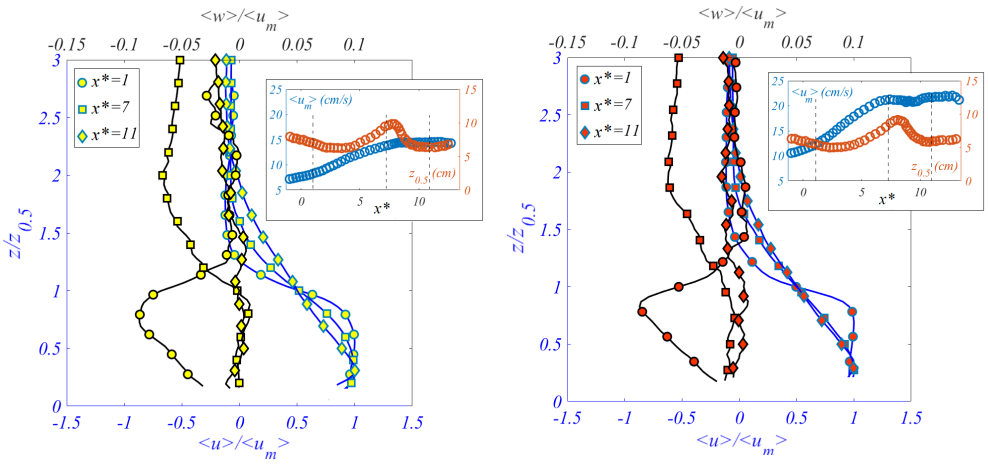

(a) (b)

Figure 4: Dimensionless profiles of the averaged streamwise velocity $\langle u\rangle/\langle u_m\rangle$ and vertical velocity $\langle w\rangle/\langle u_m\rangle$ for the experiments $R5_2$ (a) and $R15_3$ (b). The insets show time-average maximum values of the streamwise velocity component $\langle u_m\rangle$ in blue and the $z_{0.5}$ in red with the vertical continuous lines indicating the positions $x^* = 1, 7$ and 11.

and $z_{0.5}$ are shown in blue and orange respectively in the insets at the top right in Fig.4(a) and (b). Both experiments show a similar trend of $z_{0.5}$ and $\langle u_m\rangle$. In accordance with what was mentioned already above, it can be seen (compare insets) that higher g_0' and q_0 lead to a higher $\langle u_m\rangle$, which increases along x^* until it reaches an almost constant value at $x^* > 7$. The change in $z_{0.5}$ is more complex. Upstream of the slope, $z_{0.5}$ is nearly constant while at slope begin first decreases and then increases smoothly in the deepest part of the slope due to the formation of KHI. Toward the end of the slope there is a rapid decrease of $z_{0.5}$ toward a constant value. As expected, the dimensionless velocity distributions and values are practically the same in experiments $R5_2$ and $R15_3$.

Calculating entrainment is of interest because it expresses mixing with the ambient fluid, related with interfacial instability, and interfacial drag. Following Morton et al. (1956), entrainment of ambient fluid is related with the normal velocity w_h at the interface with the entrainment coefficient defined by:

$$E_w = -\frac{w_h}{U}, \tag{2}$$

where U is the depth integrated velocity of the current. A cross-stream location $z/z_{0.5} \approx 1.5$ has been chosen as the interface. Then, the velocity w_h at this location has been obtained from the PIV velocity data (Fig 3 and 4) by taking the average of three values of the normal velocity around $z/z_{0.5} = 1.5$. Invariance of the results has been checked by comparison between results obtained directly from averaged velocity fields and from instantaneous velocity fields. We note that, as already reported by Odier et al. (2014) and Martin et al. (2019) this definition of entrainment coefficients gives values somewhat larger than those obtained with the definition using the volume flux change in the downstream direction, $E_q = 1/Ud(Uh)/dx$ (cf. also Fig. 6).

Fig.5a shows the time-averaged entrainment coefficients E_w versus x^* for $R5_2$, $R15_2$ and $R15_3$ experiments. Despite the different initial conditions, E_w shows a similar behavior in all experiments. The entrainment rates are almost zero during the initial acceleration phase ($0 < x^* < 2$) and increase rapidly as KHI develop to reach maximum values at the steepest part of the slope ($x^* \approx 7$) and then decreases again in the TSL region. To highlight the effect of slope variation on entrainment, Fig.5(b-d) report the entrainment E_w evaluated at $x^* = 1$(b), $x^* = 7$(c) and $c^* = 11$(d) as a function of the injected buoyancy flux B_0 for all the performed experiments.

In Fig.6 the entrainment coefficient E_w and E_q are plotted as a function of the local Froude number $Fr = Ri_g^{-0.5}$ and compared with other experimental data. The present data are for the range $0.5 < x^* < 1.5$, $6.5 < x^* < 7.5$ and $10.5 < x^* < 11.5$ and for experiments in which both velocity and density field measurements are available. To compute the Froude number, the gradient Richardson number $Ri_g = N^2 \cos\theta / S^2$ ($Fr = 1/\sqrt{Ri_g}$) has been used, where $N = \sqrt{-g\langle\delta_z\rho\rangle/\langle\rho\rangle}$ and $S = \langle\delta_z u\rangle$ represent the Brunt-Väisäla frequency and the vertical shear of velocity, respectively. We see that the data of the present study are in good agreement with those of previous studies.

3.2. Reynolds stresses

Key quantities for describing turbulence processes are the Reynolds stresses expressing turbulent transport of momentum (Gray et al., 2006). Fig.7 displays the variation with $z/z_0.5$ of the time averaged Reynolds stresses $\langle u'u'\rangle/\langle u_m^2\rangle$, (a,b) and of $\langle w'w'\rangle/\langle u_m^2\rangle$ (c,d) at $x^* = 7$ and $x^* = 11$ for experiments $R5_2$, $R15_2$ and $R15_3$. As expected, low values are observed close to the velocity maximum, increasing toward the wall (in the boundary layer, not shown here) and values are maximum in the outer shear layer (Kneller et al., 1997; Cantero et al., 2008).

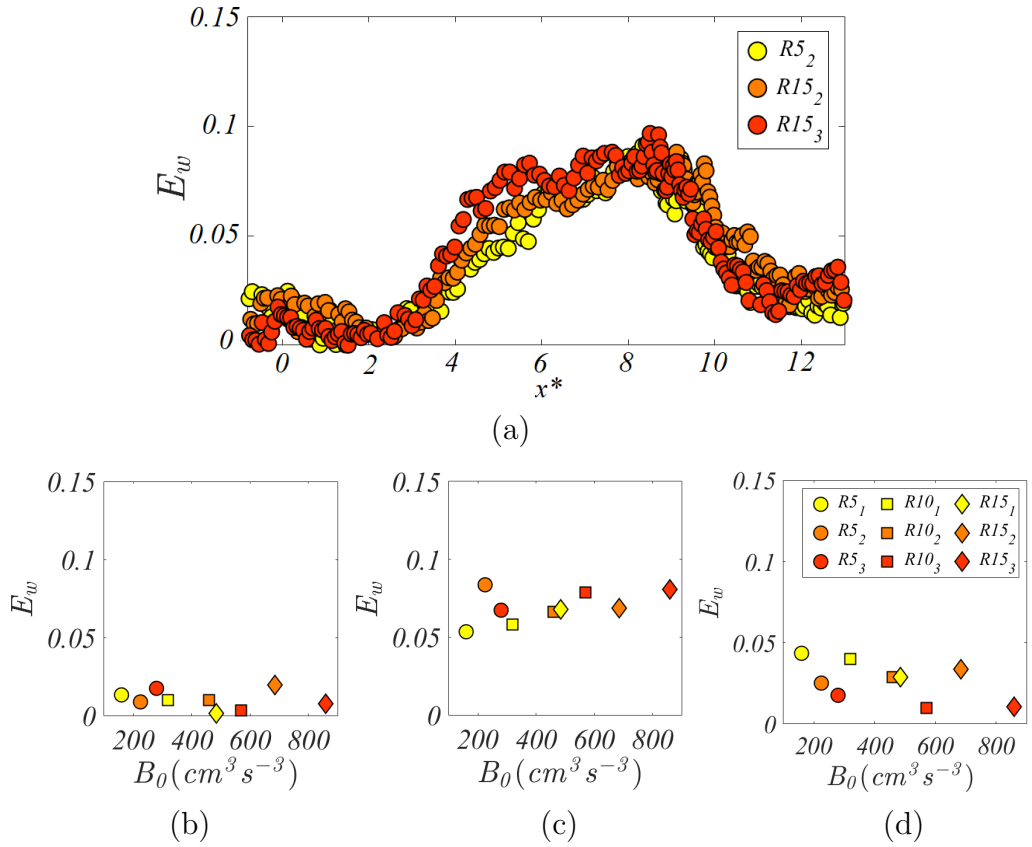

Figure 5: a) Time-averaged entrainment coefficients E_w versus x^* for experiments $R5_2$, $R15_2$ and $R15_3$. Entrainment coefficient E_w versus initial buoyancy flux B_0, at $x^* = 1$ (b), $x^* = 7$ (c) and $x^* = 11$ (d) for all performed experiments.

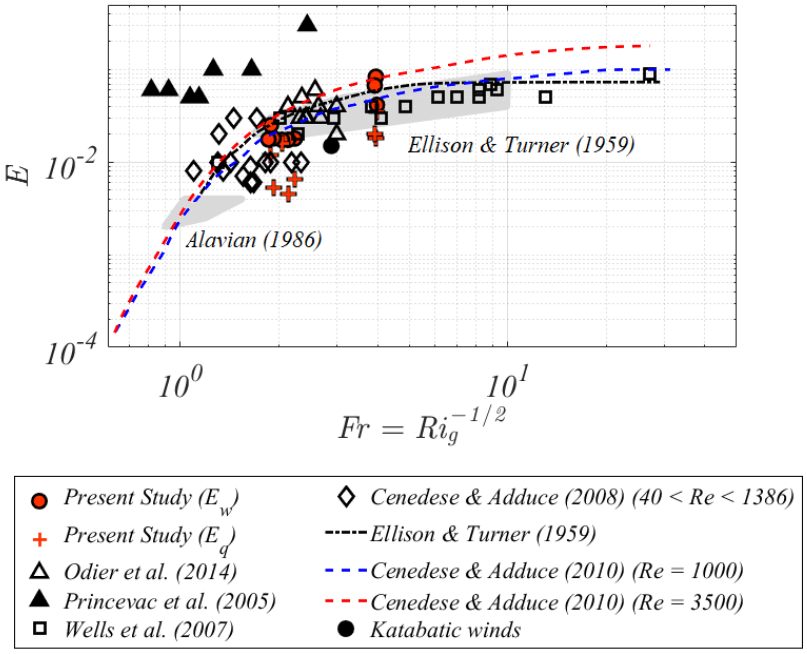

Figure 6: Entrainment coefficients, E_w (red $\circ$), and E_q (red $+$) as a function of the local Froude number $Fr = Ri_g^{-1/2}$. Present entrainment coefficients are for the range $0.5 < x^* < 1.5$, $6.5 < x^* < 7.5$ and $10.5 < x^* < 11.5$ of all experiments with $g_0' = 5cms^{-2}$. Data of E_w from Odier et al. (2014), Princevac et al. (2005), Wells et al. (2010), Cenedese and Adduce (2008) and Charrondière et al. (2022) (katabatic winds in situ measurements) are included for comparison. Shaded areas represent laboratory experiments of Alavian (1986) and Ellison and Turner (1959) with the black dashed line representing the classical variation of Ellison and Turner (1959) and the dashed blue and red lines the variation as reported in Cenedese and Adduce (2010).

The maximum values of the normal Reynolds stresses $\langle u'u' \rangle / \langle u_m^2 \rangle$ and $\langle w'w' \rangle / \langle u_m^2 \rangle$ at $x^* = 7$ have a near Gaussian distribution and are located close to $z/z_{0.5} = 1$ (see Fig.7a,c). In the experiments with larger density difference ($R15_{2,3}$), the values are lower and more spread out. The explanation for this behaviour is the difference in the mean velocity profiles. In experiment $R5_2$ the profile above maximum velocity is similar to that of a mixing layer i.e. of erf type (Pope, 2000), whereas when g_0' is larger, higher acceleration due to larger gravitational force, gives rise to a wider region of nearly constant shear and consequently constant normal stresses. Stratification has practically no effect on Reynolds stresses at $x^* = 7$, the gradient Richardson number being small (of order 0.1). At $x^* = 11$ a region of nearly constant shear exists in all three experiments, hence nearly constant normal stresses over this region. Maximum values of the Reynolds stresses are about half of those at $x^* = 7$ due to the collapse of KHIs and re-stratification process that takes place at the end of the slope.

The Reynolds shear stresses $\langle u'w' \rangle$ are shown in Fig. 8, with the instantaneous two-dimensional field of the scaled Reynolds shear stresses $\langle u'w' \rangle$ along x^*, of experiment $R5_2$, presented in Fig. 8a. As previously observed (Martin et al., 2019), in the HI region the largest fluctuations are concentrated at the sheared interface only. As the current develops down the slope, an increase of the shear stresses is observed due to acceleration and rapid onset of the KHI, which spread over the full current depth: large values of $\langle u'w' \rangle / \langle u_m^2 \rangle$ characterize the full shear layer with the largest values on the steepest part of the slope at $x^* = 7$ where $\theta = 31°$. This is highlighted in Fig.8b and Fig.8c where scaled Reynolds shear stress profiles, computed at $x^* = 7$ and $x^* = 11$, respectively, are reported. In accordance with the behaviour of the normal stresses, at $x^* = 7$ there is a clear maximum in experiment $R5_2$, located at the sheared interface close to $z/z_{0.5} = 1$ whereas when g_0' is larger, maximum values are lower and spread out. Furthermore, at $x^* = 11$ where there is a general decrease of the turbulent fluctuations, the shear stress values are less than half of those at $x^* = 7$.

Odier et al. (2012) proposed a novel method for characterizing the distribution of correlations of the velocity fluctuations to better understand the mixing process based on the probability density functions (PDFs) of the momentum fluxes $\langle u'w' \rangle$. Fig.9 shows the PDFs of $\langle u'w' \rangle$ in the range $8.5 < x^* < 11.5$ of experiment $R15_2$. Each PDF is obtained using data in a normal band of $1cm$ height, starting from the bottom of the slope, and is highlighted with a different color enabling to see the evolution of the PDFs as

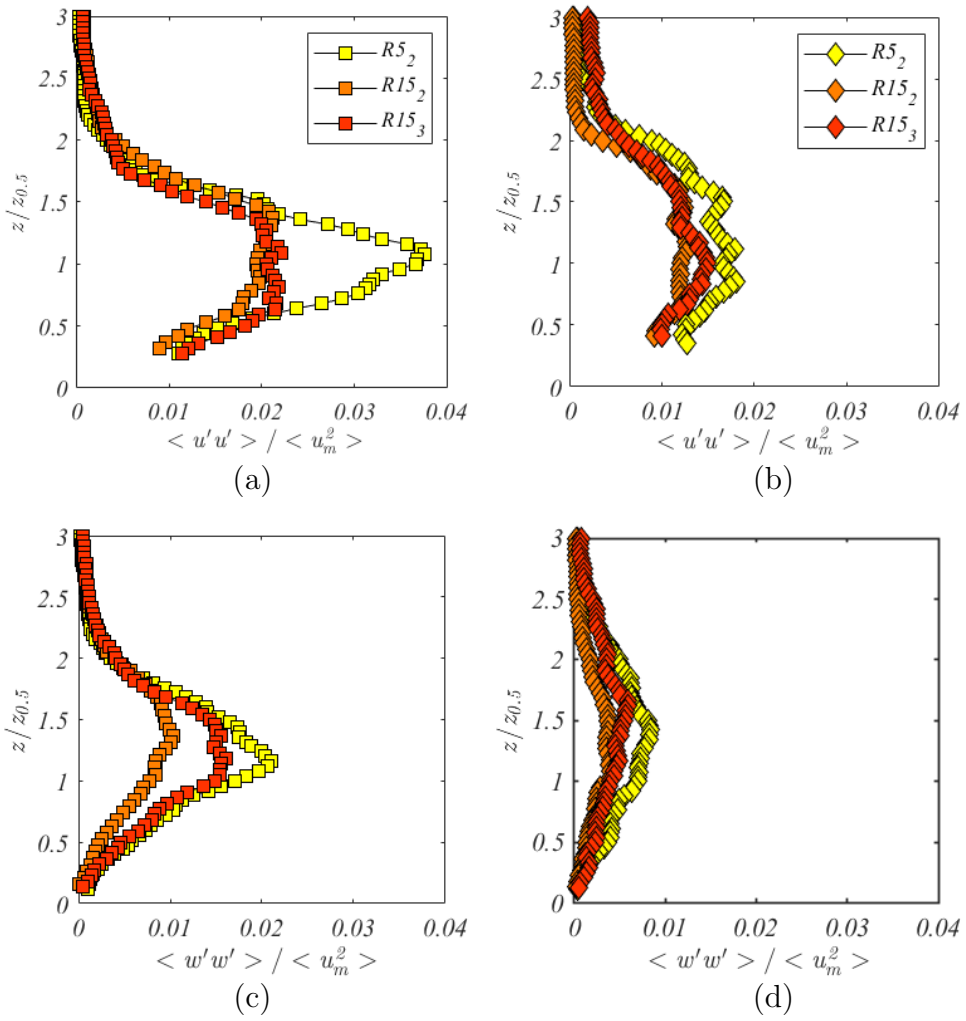

Figure 7: Scaled normal Reynolds stress profiles determined at $x^* = 7$ (a,c) and $x^* = 11$ (b,d) in experiments $R5_2$, $R15_2$ and $R15_3$.

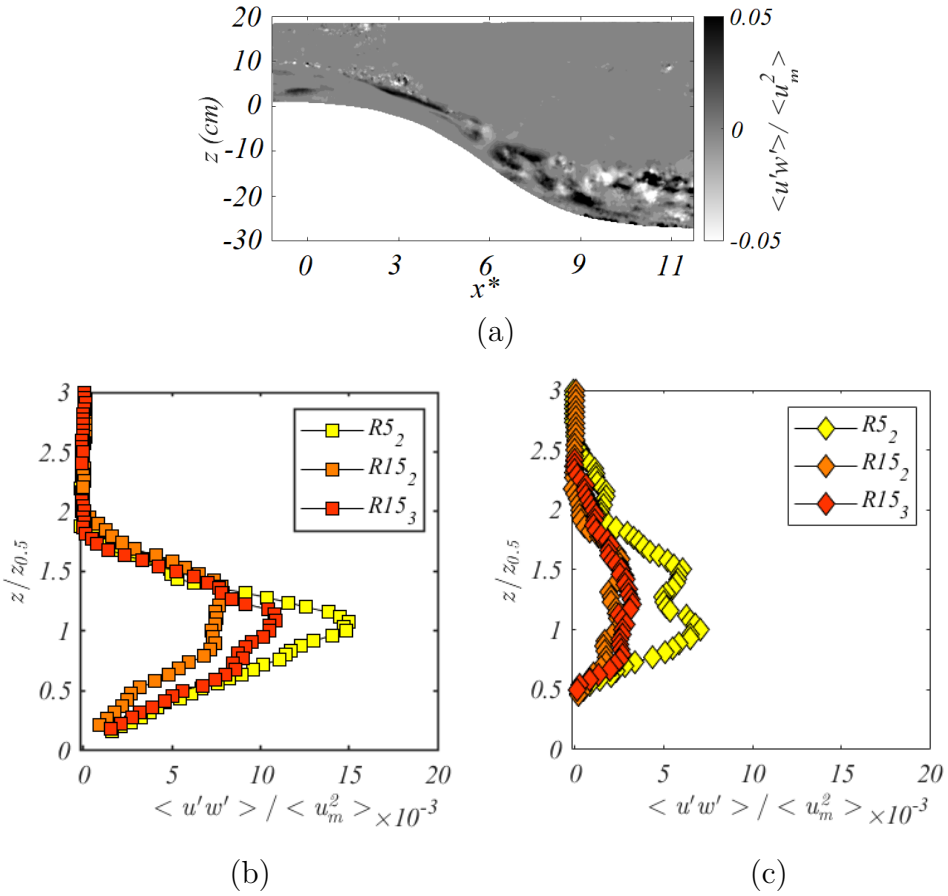

Figure 8: (a) Scaled instantaneous Reynolds shear stresses $\langle u'w' \rangle \langle u_m^2 \rangle$ along x^* of experiment $R5_2$. Profiles of scaled Reynolds shear stresses at $x^* = 7$ (b) and at $x^* = 11$ (c) in experiments $R5_2$, $R15_2$ and $R15_3$.

the vertical distance increases. As also seen in Fig. 8, the fluxes reach nearly 2% of the squared maximum velocity flow so as there is still a probability (10^{-3}) that a fluctuation will reach a value about 15 times the mean (Fig.9). Usually, as the center of the mixing region is approached, i.e. the interface between the current and the ambient fluid, large fluctuations are present and the PDFs of the momentum fluxes are asymmetric (Odier et al., 2012). This asymmetry is the origin of the non-zero mean value of the fluxes indicating either downward transport (entrainment) of downstream momentum or upward transport of upstream momentum, according to the mixing mechanism induced by the KHI. This behavior is not observed in our analysis, since the PDF were evaluated on the TSL area where the stratification is interrupted by the collapse of the KHIs.

3.3. Mixing length and shear scale

Reynolds stresses can be conceptually parameterised by an eddy or turbulent viscosity, $K_m = -\langle u'w' \rangle / \partial_z u$, that relates chaotic fluid motion to diffusive type processes (Pope, 2000; Mukherjee and Balasubramanian, 2020). It is a useful parameter for indicating the extent of internal mixing and is used extensively in both numerical and analytical modelling of turbulent flows.

Based on the mixing length model proposed by Prandtl (1927), the Reynolds stresses $\langle u'w' \rangle$ can also be related to the square of the velocity gradient $\langle \partial_z u \rangle^2$ using a proportionality constant which represents a mixing length L_m:

$$L_m^2 = \frac{\langle u'w' \rangle}{\langle \partial_z u \rangle^2} \,, \tag{3}$$

Fig.10 shows the computed vertical profiles of the turbulent eddy diffusivity K_m (a,b) and mixing lengths L_m (c,d) at $x^* = 7$ and $x^* = 11$ (left and right columns, respectively). The corresponding z variation of mean velocity gradients $\partial_z u$ are presented in the insets. Data close to the bottom and top extremities are not reported because experimental errors become large. L_m is computed starting at a distance from the wall of approximately 20% of the current depth (Pope, 2000).

At $x^* = 7$ (Fig.10c), mixing lengths L_m are nearly constant in experiments $R15_2$ and $R15_3$. while eddy coefficients increase and then decrease with distance z. When density differences are lower ($R5_2$), both, L_m and K_m behave differently in the lower part because of the difference in velocity gradient. In general, close to the velocity maximum and at large distances from the bottom, the vertical derivative $\partial_z u$ becomes almost zero, so that

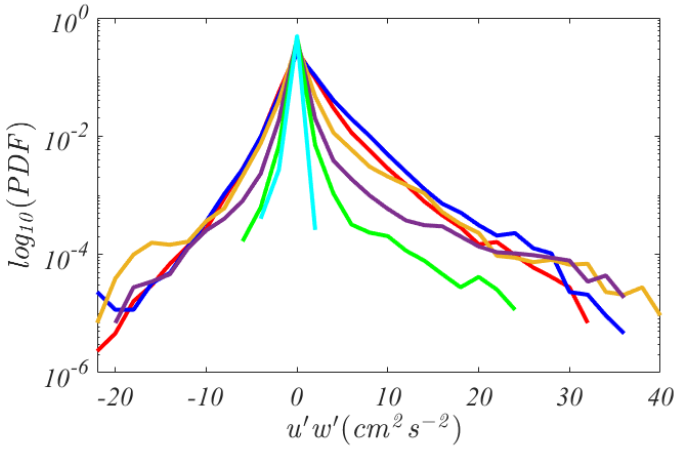

(a)

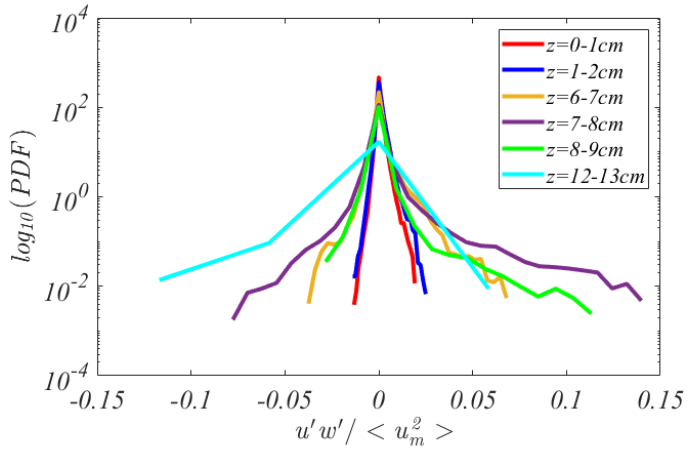

(b)

Figure 9: PDFs of instantaneous shear stress (a), and of scaled shear stress (b) in $R15_2$ experiment. Each PDF is constructed using data in a band of 1cm height from the bottom (normal position indicated in the legend), situated in the TSL area at $8.5 < x^* < 11.5$.

large fluctuations in the calculated L_m occur at these extremities. Averaging over the depth and the downstream distance in the considered region, gives a mean value of $L_m \approx 0.60 \pm 0.1$, which compares well with those reported by Odier et al. (2009) of $L_m \approx 0.45 \pm 0.1$.

At the end of the slope in the TSL region ($x^* = 11$) (Fig.10b) the values of L_m and of K_m are lower and both increase almost linearly with $z/z_{0.5}$. This is probably related with the substantially lower and nearly constant Reynolds stresses at this location.

In order to understand how mixing lengths and eddy coefficients depend on the effect of turbulent kinetic energy, of stable stratification, and of destabilization by shear it is useful to determine the shear scale L_s and the buoyancy length (Ozmidov scale) L_o, which are defined as (Bluteau et al., 2013; Odier et al., 2014):

$$L_s = \sqrt{\frac{\overline{\epsilon}}{\overline{\langle \partial_z u \rangle^3}}}\,, \qquad L_o = \sqrt{\frac{\overline{\epsilon}}{\left(g\frac{\overline{\langle \partial_z \rho \rangle}}{\langle \overline{\rho} \rangle}\right)^{3/2}}}, \tag{4}$$

where $\overline{\langle \cdot \rangle}$ represents a time average over the experimental duration and $\overline{\epsilon}$ the mean turbulent dissipation rate. As already pointed out by Odier et al. (2012), the smaller of these scales limits the mixing length L_m, hence, also K_m. The strength of stratification with respect to the shear is measured by the (gradient) Richardson number Ri_g which also relates these two scales via the relation $L_s/L_o = {Ri_g}^{3/2}$. Generally, gravity currents on slopes are characterized by low Richardson numbers $Ri_g \ll 1$, hence shear dominates over stratification so that the shear scale L_s is expected to limit the mixing length L_m and K_m.

According to Kolmogorov's similarity hypothesis, the dissipation is the only flow variable that characterizes the state of turbulence when stratification is weak. The significance of ϵ has been extensively addressed in numerous studies (Antonia and Pearson, 2000; Doron et al., 2001; Xu and Chen, 2013). Following Steinbuck et al. (2010) and Xu and Chen (2013) the dissipation rate can be estimated using the four resolved velocity gradients obtained by PIV as:

$$\epsilon = \nu\langle 4(\partial_x u')^2 + 4(\partial_z w')^2 + 3(\partial_z u')^2 + 3(\partial_x w')^2 + 4(\partial_x u' \partial_z w') + 6(\partial_z u' \partial_x w')\rangle \tag{5}$$

In a stratified flow the dissipation is equal to production minus the loss of energy to buoyancy. In a flow on a slope there is, in addition to shear

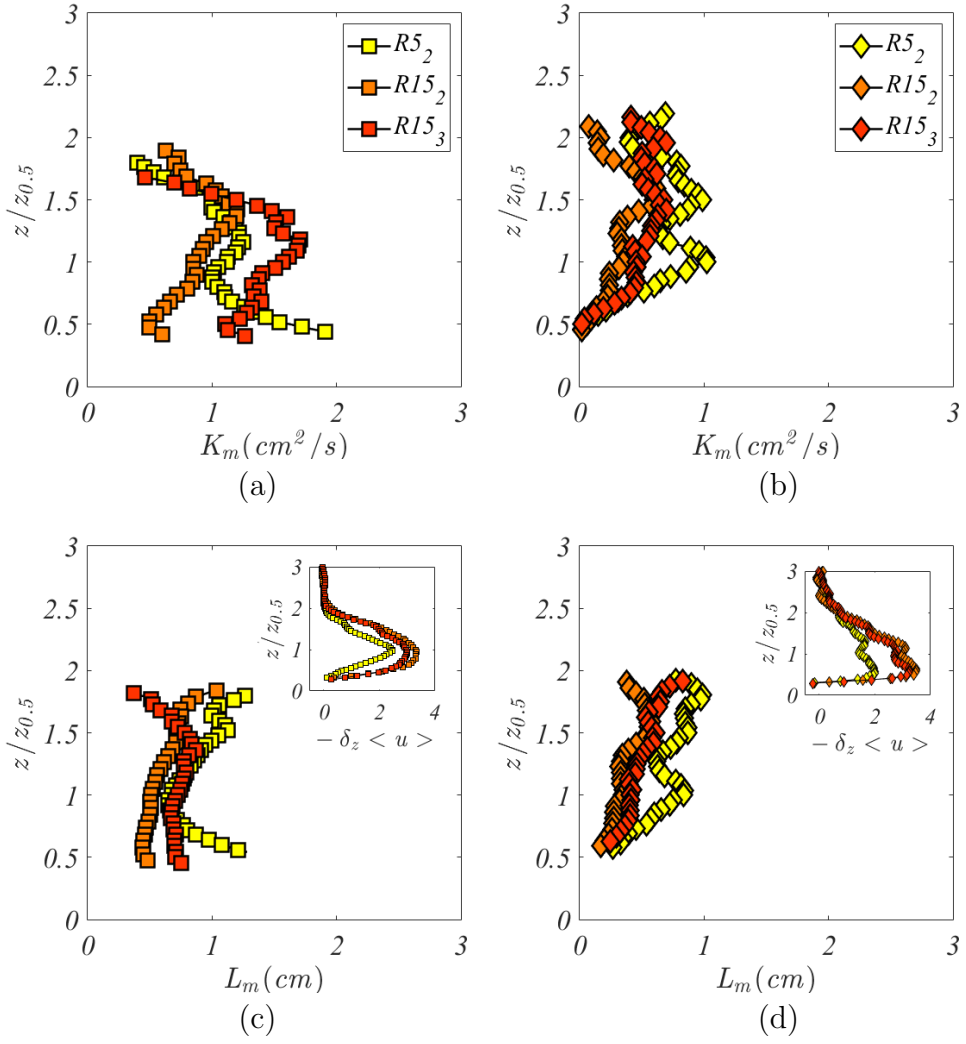

Figure 10: Variations of eddy coefficient K_m and mixing lengths L_m with $z/z_{0.5}$ at $x^* = 7$, (a,c) and at $x^* = 11$, (b,d). Close to the velocity maximum, as well as far away from it, the $\partial_z u$ tend to vanish, producing large fluctuations in K_m and L_m. The insets show the velocity gradients $\partial_z u$ as a function of $z/z_{0.5}$.

production, also TKE production by buoyancy. Neglecting advection and diffusion terms, the TKE energy balance is given by:

$$-\overline{u'w'}\frac{\partial u}{\partial z} - \frac{g}{\rho}\overline{w'\rho'}\cos\theta + \frac{g}{\rho}\overline{u'\rho'}\sin\theta \approx \epsilon \tag{6}$$

The buoyancy terms are opposite in sign with the ratio of $\frac{g}{\rho}\overline{w'\rho'}\cos\theta$ to shear and buoyancy production (mixing efficiency) being ≈ 0.1 and $\overline{u'\rho'}\sin\theta/\overline{w'\rho'}\cos\theta \leq 1$ when $Ri_g < 0.1$ (Charrondière et al., 2022); hence $\epsilon \approx \overline{w'u'}\partial_z u$. The production is maximum near $z/z_{0.5}$ whereas, because of diffusion and advection terms, dissipation is more uniformly distributed across the outer region of the current and is close to the average of the production, i.e.:

$$\overline{\epsilon} \approx 0.6(\overline{w'u'}\partial_z u)_{max}. \tag{7}$$

The value of ϵ computed from equation (5) is nearly up to an order of magnitude less than $\overline{\epsilon}$ from equation (7). To estimate the dissipation rate ϵ directly from the PIV data and avoid important underestimations, it is necessary to have a spatial resolution of the PIV close to the Kolmogorov scale η_K. The spatial resolution of the present PIV measurements is $3mm$, while $\eta_K = \nu^3/\epsilon^4$ is of the order of $\mathcal{O} \sim 0.4mm$ estimated using $\epsilon = u'^3/h$ (Tennekes et al., 1972). Hence the direct calculation of ϵ from the PIV data using equation (5) will considerably underestimate the dissipation. To calculate the values of L_s we use the z variation given by equation (5) with a pre-factor such that the maximum of ϵ is close to $\overline{\epsilon}$ of equation (7).

Fig.11 shows the measured mixing length L_m versus the computed shear scale L_s and K_m versus $L_s^2\delta_z u$ for all the experiments performed. The experimental data of the present study all are close to or fall above the dashed straight line in Fig.11 representing $L_m = L_s$ $K_m = L_s^2\delta_z u$, which is different from the results of Odier et al. (2012) where $L_m < L_s$. A possible explanation for the difference is the non-constant and much steeper bottom slope θ in the present experiments that can have important consequences on the mixing properties.

4. Comparison with katabatic winds

Studies of katabatic winds are numerous (see for instance (Princevac et al., 2008; Charrondière et al., 2022) because these flows affect local weather conditions causing also temperature inversion in valleys that are prone to pollution. In Antarctica and Greenland, katabatic winds are directly responsible

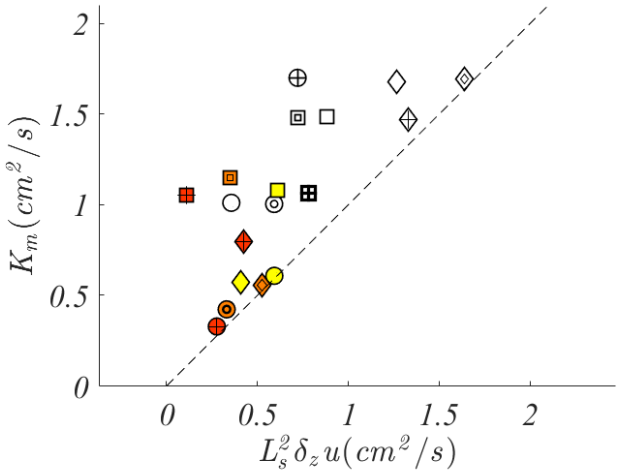

(a)

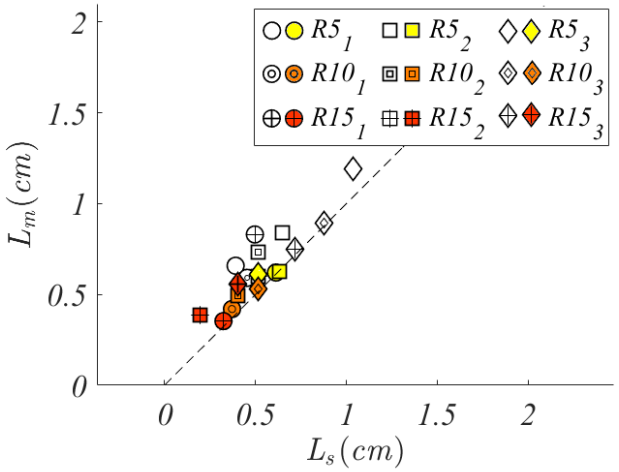

(b)

Figure 11: Eddy coefficient K_m versus $L_s^2\delta_z u$ and mixing length L_m versus computed shear length L_s, for all the experiments performed at $x^* = 7$ (empty markers) and $x^* = 11$ (filled markers).

Table 2: Characteristic turbulence length scales of present experiments of Odier et al. (2012) and in katabatic flows (Charrondière et al.). The dissipation ϵ has been computed using equations (5) and (7). $\triangle z = \triangle u / \partial_z u_{z0.5}$ is the shear thickness.

Run	$\langle\epsilon\rangle$	L_m	L_s	$\lvert\triangle z\rvert$	$z_{0.5}$
$R15_2(x^*=7)$	$6.8\text{cm}^2\text{s}^{-3}$	0.61cm	0.51cm	6.0cm	6.8cm
$R15_2(x^*=11)$	$1.0\text{cm}^2\text{s}^{-3}$	0.38cm	0.20cm	7.5cm	5.6cm
$R15_3(x^*=7)$	$9.0\text{cm}^2\text{s}^{-3}$	0.75cm	0.72cm	7.0cm	8.0cm
$R15_3(x^*=11)$	$2.8\text{cm}^2\text{s}^{-3}$	0.55cm	0.40cm	9.9cm	5.9cm
Charrondière et al.					
z=0.66m	$5.7 \cdot 10^3\text{m}^2\text{s}^{-3}$	0.09m	0.21m	11.1m	3.7m
z=0.98m	$5.5 \cdot 10^3\text{m}^2\text{s}^{-3}$	0.16m	0.21m	11.1m	3.7m
z=1.50m	$5.2 \cdot 10^3\text{m}^2\text{s}^{-3}$	0.26m	0.27m	11.1m	3.7m
z=1.93m	$4.4 \cdot 10^3\text{m}^2\text{s}^{-3}$	0.35m	0.32m	11.1m	3.7m
z=2.37m	$4.0 \cdot 10^3\text{m}^2\text{s}^{-3}$	0.45m	0.39m	11.1m	3.7m
z=9.77m	$4.6 \cdot 10^4\text{m}^2\text{s}^{-3}$	1.16m	1.2m	11.1m	3.7m
Odier et al. (2012)					
	$0.5 \div 1.4\text{cm}^2\text{s}^{-3}$	$0.2 \div 0.6$cm	$0.15 \div 0.7$cm	$1.6 \div 6.8$cm	

for cooling the ocean surface water at the polynya (Maqueda et al., 2004) and open sea and play an important role for the deep water formation. Katabatic flows are driven by buoyancy supply from the ground (ground cooling), whereas in most laboratory currents buoyancy flux is constant and equal to the upstream buoyancy supply, hence, the flow structure is expected to be different. A formal comparison is, nevertheless, of interest. Ellison and Turner (1959) for instance evaluated the mean flow development of katabatic winds using their results of a buoyancy conserving gravity current on a slope. The recent detailed field measurements by Charrondière et al. (2020, 2021, 2022) on steep alpine slopes of 30° inclination (Grand Colon, Belledonne chain) provide an excellent data set for comparing katabatic jets data, including turbulent mixing, with laboratory gravity currents results. The shape and slope inclination adopted in the present study reproduces a typical alpine topography in the French Alps and specifically the Grand Colon topography.

Fig.12a shows a comparison of the slope normal katabatic wind mean velocity profile during a representative katabatic event on February 24th 2019 (5h-8h) with a slight up-slope wind of velocity $U_a = -0.2m/s$, with the $R15_3$ experimental mean velocity. The errors bars on the katabatic velocity profile

show the variability of the mean wind during the katabatic event, while the black dashed line represents the fit derived from the Prandtl model (Brun et al., 2017). The velocity profiles are quite different: indeed in katabatic winds the velocity distribution above maximum velocity has a logarithmic trend with maximum gradient close to the velocity maximum whereas in laboratory experiments the maximum gradient is located near the current mid-height. The explanation for this difference are the very different density distributions, as presented in Fig.12b. In the constant, upstream buoyancy supply of laboratory gravity currents, the excess density decreases over the whole flow depth, whereas in the katabatic wind (buoyancy supply from the boundary) the density variation is located in the lower $10-20\%$ of the gravity flow. In spite of this considerable difference in mean flow, in addition to the large difference in Reynolds number, entrainment coefficients lie within the bulk of laboratory currents as is seen in Fig.6.

To compare turbulence quantities, notably mixing lengths L_m and K_m, with those obtained in katabatic winds, extended to larger z values given in Charrondière et al. (cf. Tab.2), a characteristic length scale is required for making L_m, K_m as well as L_s dimensionless. An appropriate length scale is $\triangle z = \triangle u/\partial_z u_{z0.5}$, that collapses all the data reasonably well as is shown in Figs.12(c,d), where in (c), $K_m/\triangle z \triangle u$ are plotted as a function of $L_s^2/\triangle u^2$ and in (d), mixing lengths $L_m/\triangle z$ as a function of $L_s/\triangle z$. Both, the scaled K_m and L_m increase with L_s to reach an upper limit of $K_m/\triangle z \triangle u \approx 0.008$ and $L_m/\triangle z \approx 0.1$. Interestingly, these maximum values of dimensionless eddy coefficients and mixing lengths are similar to that of a turbulent boundary layer where $L_m/\delta \approx 0.1$ (the shear thickness $\triangle z$ is the equivalent of δ). In terms of bottom friction velocity, $u_\tau \approx 0.07 u_m$ (Charrondière et al., 2022), where here $u_m = \triangle u$, $K_m/\triangle z u_\tau \approx 0.1$, and which is close to the maximum value in a turbulent boundary layer (Pope (2000), p.307). However, the variations of eddy coefficients and mixing lengths with L_s, have quite different origins. In katabatic flows, these are a function of height z with values increasing from nearly zero up to the maximum value, whereas in the constant buoyancy flux gravity current, the mixing length is practically constant along z. The change seen in Figs.12(c,d) is due to a change with position x, i.e. values are maximum at $x* = 7$ and lower at $x* = 11$. The eddy coefficient varies with z and with x. This notable difference with katabatic winds is due to the widely different mean velocity profiles.

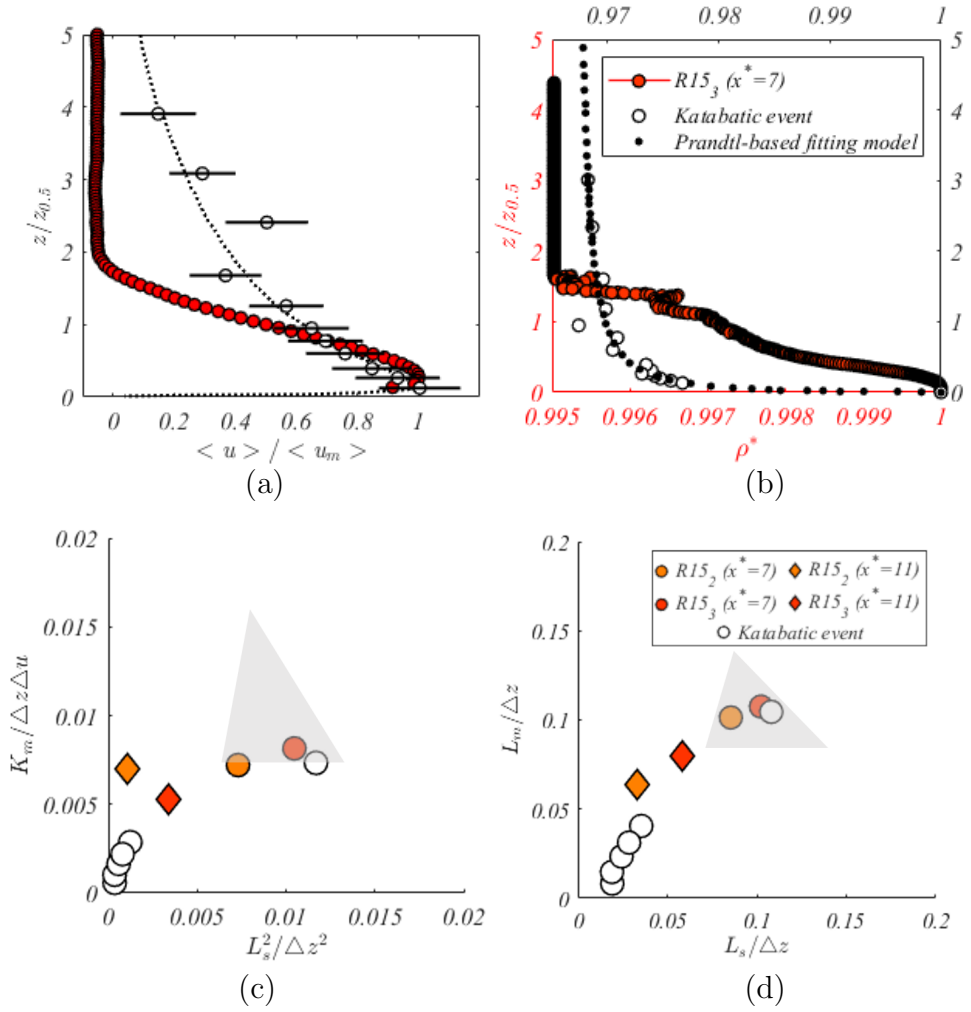

Figure 12: Dimensionless profiles of mean streamwise velocity, (a) and of density, (b), at $x^* = 7$ in experiment $R15_3$ compared with katabatic wind profiles of 2019B event in (Charrondière et al., 2022) . Dimensionless eddy coefficients K_m, (c), and mixing lengths L_m (d), versus dimensionless shear length L_s.

The shaded gray area represents the values of Odier et al. (2012).

5. Summary and concluding remarks

The constant buoyancy flux gravity currents flowing from horizontal onto a steep, hyperbolic tangent shaped slope that is representative of an alpine topography, reveal novel features. The current accelerates down the slope, while downstream, on the horizontal boundary, the velocity remain nearly unchanged because both the gravitational force and entrainment are drastically reduced. The interfacial instability changes from Holmboe instability (HI) near slope begin to Kelvin-Helmholtz (KHI) on the steepest part of the slope, where $Ri_g \approx 0.1$ and entrainment is large, followed by turbulence collapse, i.e. a stable turbulent shear layer (TSL), where $Ri_g \approx 0.3$ and entrainment ceases.

The computed Reynolds stresses are maximum in the central part of the interface with the distribution depending on the buoyancy flux. In the TSL region Reynolds stresses are more spread out. Mixing lengths determined via the correlation terms between fluctuating components of the velocity field at the location of the steepest slope ($x^* = 7$) and at a downstream position in the turbulent shear layer (TSL) region ($x^* = 11$) are pratiacally constant across the shear zone whereas eddy coefficients vary with height. Both scale closely with the shear scale, in agreement with Odier et al. (2012). The comparison between the present saline gravity current experiments and of field data, obtained in katabatic winds on alpine slopes, highlights the very different mean flow structures. However, the mixing lengths and the eddy coefficients data agree surprisingly well and collapse when using an appropriate scaling which has been defined as ($\triangle z = \triangle u/\partial_z u_{z0.5}$), even though Reynolds numbers between the laboratory and the observational data differ at least of two orders of magnitude. An upper limit of mixing length and eddy coefficient is reached at a certain value of the shear scale, corresponding to a certain height in katabatic winds.

Reproducing katabatic wind conditions in the laboratory would be of interest for the understanding of certain important aspects of these flows. It is for instance well documented that katabatic winds exhibit mean flow oscillations (McNider, 1982; Princevac et al., 2008; Charrondière et al., 2022) and it has been speculated that these oscillations are related with ambient stratification. Thus, experiments with saline gravity currents in the presence of ambient stratification could help in clarifying the underlying mechanism of these oscillations. As a further step, simulating katabatic flow conditions in the laboratory, by injecting a saline solution through a porous bottom bound-

ary or by cooling it, would allow to study the spatial mean flow development and related mixing characteristics proper of katabatic flows.

Acknowledgements

The authors are very grateful to Claudine Charrondiere for making available the katabatic wind in situ data and for fruitful discussions. Special thanks go to Joseph Virone and Vincent Govart for their technical support in preparing the experiments. Financial support was given by a grant from Labex OSUG@2020 (Investissements d'avenir ANR10 LABX56).

Declaration of Interests

The authors report no conflict of interest.

Author Statement

We hereby declare and confirm that all the authors have substantially contributed to the work, and have read and approved the submitted manuscript.

References

Agrawal, T., Ramesh, B., Zimmerman, S., Philip, J., Klewicki, J.C., 2021. Probing the high mixing efficiency events in a lock-exchange flow through simultaneous velocity and temperature measurements. Phys. Fluids 33, 016605. doi:10.1063/5.0033463.

Alavian, V., 1986. Behavior of density currents on an incline. Journal of hydraulic engineering 112, 27–42.

Antonia, R., Pearson, B., 2000. Effect of initial conditions on the mean energy dissipation rate and the scaling exponent. Physical Review E 62, 8086.

Baines, P.G., 2005. Mixing regimes for the flow of dense fluid down slopes into stratified environments. Journal of Fluid mechanics 538, 245–267.

Balasubramanian, S., Zhong, Q., 2018. Entrainment and mixing in lock-exchange gravity currents using simultaneous velocity-density measurements. Physics of Fluids 30, 056601.

Bluteau, C., Jones, N., Ivey, G., 2013. Turbulent mixing efficiency at an energetic ocean site. Journal of Geophysical Research: Oceans 118, 4662–4672.

Brun, C., Blein, S., Chollet, J.P., 2017. Large-eddy simulation of a katabatic jet along a convexly curved slope. part i: Statistical results. Journal of the Atmospheric Sciences 74, 4047–4073.

Buckee, C., Kneller, B., Peakall, J., 2001. Turbulence structure in steady, solute-driven gravity currents. Particulate gravity currents , 173–187.

Cantero, M.I., Balachandar, S., García, M.H., Bock, D., 2008. Turbulent structures in planar gravity currents and their influence on the flow dynamics. Journal of Geophysical Research: Oceans 113.

Cenedese, C., Adduce, C., 2008. Mixing in a density-driven current flowing down a slope in a rotating fluid. J. Fluid Mech. 604, 369–388.

Cenedese, C., Adduce, C., 2010. A new parameterization for entrainment in overflows. J. Phys. Oceanogr. 40, 1835–1850.

Charrondière, C., Brun, C., Cohard, J.M., Sicart, J.E., Obligado, M., Biron, R., Coulaud, C., Guyard, H., 2021. Katabatic winds over steep slopes: overview of a field experiment designed to investigate slope-normal velocity and near-surface turbulence. Boundary-Layer Meteorology , 1–26.

Charrondière, C., Brun, C., Hopfinger, E.J., Cohard, J.M., Sicart, J.E., 2022. Mean flow structure of katabatic winds and turbulent mixing properties. Journal of Fluid Mechanics 941.

Charrondière, C., Brun, C., Sicart, J.E., Cohard, J.M., Biron, R., Blein, S., 2020. Buoyancy effects in the turbulence kinetic energy budget and reynolds stress budget for a katabatic jet over a steep alpine slope. Boundary-Layer Meteorology 177, 97–122.

Charrondière, C., Hopfinger, E.J., Brun, C., . Identification of k_x^{-1} strong wave turbulence and of $k_x^{-7/5}$ temperature spectral ranges in katabatic winds on a steep slope. Journal of Fluid Mechanics. (Accepted) .

Cuthbertson, A., Laanearu, J., Carr, M., Sommeria, J., Viboud, S., 2018. Blockage of saline intrusions in restricted, two-layer exchange flows across a submerged sill obstruction. Environmental Fluid Mechanics 18, 27–57.

Dai, A., 2014. Non-boussinesq gravity currents propagating on different bottom slopes. Journal of Fluid Mechanics 741, 658–680.

Danabasoglu, G., Large, W., Briegleb, B., 2010. Climate impacts of parametrized nordic sea overflows. J. Geophys. Res. 115, C11005.

De Falco, M., Adduce, C., Maggi, M., 2021. Gravity currents interacting with a bottom triangular obstacle and implications on entrainment. Advances in Water Resources 154, 103967.

Doron, P., Bertuccioli, L., Katz, J., Osborn, T., 2001. Turbulence characteristics and dissipation estimates in the coastal ocean bottom boundary layer from piv data. Journal of Physical Oceanography 31, 2108–2134.

Ellison, T., Turner, J., 1959. Turbulent entrainment in stratified flows. J. Fluid Mech. 6, 423–448.

Eriksson, J., Karlsson, R., Persson, J., 1998. An experimental study of a two-dimensional plane turbulent wall jet. Experiments in fluids 25, 50–60.

Fernando, H., 2010. Fluid dynamics of urban atmospheres in complex terrain. Annu. Rev. Fluid Mech. 42, 365–389.

Fernando, H.J., 1991. Turbulent mixing in stratified fluids. Annual review of fluid mechanics 23, 455–493.

Gordon, A.L., Orsi, A.H., Muench, R., Huber, B.A., Zambianchi, E., Visbeck, M., 2009. Western ross sea continental slope gravity currents. Deep Sea Research Part II: Topical Studies in Oceanography 56, 796–817.

Gray, T., Alexander, J., Leeder, M.R., 2006. Longitudinal flow evolution and turbulence structure of dynamically similar, sustained, saline density and turbidity currents. Journal of Geophysical Research: Oceans 111.

Hopfinger, E., 1983. Snow avalanche motion and related phenomena. Annu. Rev. Fluid Mech. 15, 47–76.

Kneller, B., Bennett, S., McCaffrey, W., 1997. Velocity and turbulence structure of density currents and internal solitary waves: potential sediment transport and the formation of wave ripples in deep water. Sedimentary Geology 112, 235–250.

Laanaia, N., Wirth, A., Molines, J.M., Barnier, B., Verron, J., 2010. On the numerical resolution of the bottom layer in simulations of oceanic gravity currents. Ocean Sci. 6, 563–572.

Maggi, M.R., Adduce, C., Negretti, M.E., 2022. Lock-release gravity currents propagating over roughness elements. Environmental Fluid Mechanics , 1–20.

Maqueda, M.M., Willmott, A., Biggs, N., 2004. Polynya dynamics: a review of observations and modeling. Rev. Geophys. 42(1), –.

Marino, B., Thomas, L., Linden, P., 2005. The front condition for gravity currents. J. Fluid Mech. 536, 49–78.

Martin, A., Negretti, M.E., Hopfinger, E.J., 2019. Development of gravity currents on slopes under different interfacial instability conditions. Journal of Fluid Mechanics 880, 180–208.

McNider, R.T., 1982. A note on velocity fluctuations in drainage flows .

Meiburg, E., Keller, B., 2010. Turbidity currents and their deposits. Annu. Rev. Fluid Mech. 42, 135–156.

Monti, P., Fernando, H., Princevac, M., 2014. Waves and turbulence in katabatic winds. Environ Fluid Mech 14, 431–450. doi:10.1007/s10652-014-9348-1.

Morton, B., Taylor, G.I., Turner, J.S., 1956. Turbulent gravitational convection from maintained and instantaneous sources. Proceedings of the Royal Society of London. Series A. Mathematical and Physical Sciences 234, 1–23.

Mukherjee, P., Balasubramanian, S., 2020. Energetics and mixing efficiency of lock-exchange gravity currents using simultaneous velocity and density fields. Physical Review Fluids 5, 063802.

Mukherjee, P., Balasubramanian, S., 2021. Diapycnal mixing efficiency in lock-exchange gravity currents. Phys. Rev. Fluids 6, 013801.

Negretti, M., Flòr, J., Hopfinger, E., 2017. Development of gravity currents on rapidly changing slopes. J. Fluid Mech. 833, 70–97.

Negretti, M., Martin, A., Naaim Bouvet, F., 2022. On the propagation of the front speed of lock released density clouds. Adw. Water Res. .

Negretti, M.E., Zhu, D., Jirka, G., 2008. The effect of bottom roughness in two-layer flows down a slope. Dyn. Oceans Atm. 45, 46–68.

Negretti, M.E., Zhu, D.Z., Jirka, G.H., 2007. Barotropically induced interfacial waves in two-layer exchange flows over a sill. Journal of Fluid Mechanics 592, 135–154.

Nogueira, H.I., Adduce, C., Alves, E., Franca, M.J., 2013. Analysis of lock-exchange gravity currents over smooth and rough beds. J. Hydraul. Res. 51, 417–431.

Odier, P., Chen, J., Ecke, R., 2012. Understanding and modeling turbulent fluxes and entrainment in a gravity current. Physica D: Nonlinear Phenomena 241, 260–268.

Odier, P., Chen, J., Ecke, R.E., 2014. Entrainment and mixing in a laboratory model of oceanic overflow. Journal of Fluid Mechanics 746, 498–535.

Odier, P., Chen, J., Rivera, M.K., Ecke, R.E., 2009. Fluid mixing in stratified gravity currents: the prandtl mixing length. Physical review letters 102, 134504.

Ottolenghi, L., Adduce, C., Inghilesi, R., Roman, F., Armenio, V., 2016. Mixing in lock-release gravity currents propagating up a slope. Phys. Fluids 28, 056604.

Pawlak, G., Armi, L., 2000. Mixing and entrainment in developing stratified currents. Journal of Fluid Mechanics 424, 45–73.

Pope, S.B., 2000. Turbulent flows. Cambridge university press.

Prandtl, L., 1927. The generation of vortices in fluids of small viscosity. The Aeronautical Journal 31, 718–741.

Princevac, M., Fernando, H., Whiteman, C.D., 2005. Turbulent entrainment into natural gravity-driven flows. Journal of Fluid Mechanics 533, 259–268.

Princevac, M., Hunt, J.C.R., Fernando, H.J.S., 2008. Quasi-steady katabatic winds on slopes in wide valleys: Hydraulic theory and observations. J. of Atm. Sci. 65, 627 – 643. doi:10.1175/2007JAS2110.1.

Simpson, J.E., 1997. Gravity currents: In the environment and the laboratory. Cambridge University Press.

Smyth, W.D., Carpenter, J.R., Lawrence, G.A., 2007. Mixing in symmetric holmboe waves. Journal of Physical Oceanography 37, 1566 – 1583. doi:10.1175/JPO3037.1.

Steinbuck, J.V., Roberts, P.L., Troy, C.D., Horner-Devine, A.R., Simonet, F., Uhlman, A.H., Jaffe, J.S., Monismith, S.G., Franks, P.J., 2010. An autonomous open-ocean stereoscopic piv profiler. Journal of Atmospheric and Oceanic Technology 27, 1362–1380.

Tennekes, H., Lumley, J.L., Lumley, J.L., et al., 1972. A first course in turbulence. MIT press.

Wells, M., Cenedese, C., Caulfield, C., 2010. The relationship between flux coefficient and entrainment ratio in density currents. Journal of Physical Oceanography 40, 2713–2727.

Xu, D., Chen, J., 2013. Accurate estimate of turbulent dissipation rate using piv data. Experimental Thermal and Fluid Science 44, 662–672.

Zemach, T., Ungarish, M., Martin, A., Negretti, M.E., 2019. On gravity currents of fixed volume that encounter a down-slope or up-slope bottom. Physics of Fluids 31, 096604.